BACHELOR

Absorption spectroscopy on O2 production in an atmospheric pressure dielectric barrier discharge in CO2

Damen, M.A.

Award date:
2013

Technische Universiteit
Eindhoven
University of Technology

Department of Applied Physics
Plasma and Materials Processing

Absorption spectroscopy on O_2 production in an atmospheric pressure dielectric barrier discharge in CO_2

M.A. Damen

PMP 13-07

August 16, 2013

Supervisors:
dr. S. Welzel
dr. R. Engeln

Abstract

The goal of this project was to determine the amount of molecular oxygen produced by an atmospheric pressure Dielectric Barrier Discharge (DBD) in a CO_2 gas. Measurements were done on flow tubes with gap sizes of 1mm and 3mm. Absolute molecular number densities were measured using Tunable Diode Laser Absorption Spectroscopy (TDLAS) on an absorption line pair in the oxygen A-band ($b^1\Sigma_g^+ \leftarrow X^3\Sigma_g^-$), at wavelengths of 764.17nm and 764.28nm. Mixing ratios for oxygen were found between 0.03% and 1.27%, which are in good agreement with estimates based on infrared absorption studies on carbonmonoxide and ozone. These measurements confirm the assumption that only CO, O_2 and O_3 are produced as stable products by the DBD. Interestingly, the plasma reactor with a discharge gap of 3mm shows similar trends in CO_2 dissociation as established for the 1mm tube, despite their different surface to volume ratio. Futhermore, the results suggest that TDLAS on molecular oxygen provides an excellent means of monitoring the efficiency of the plasma activation process in realtime.

Contents

1. Introduction

One of the main scientific challenges of the 21st century is to replace fossil fuels with clean and sustainable energy sources. The energy demand is projected to increase in the coming years because of growing populations and projected technological development of third world countries. In principle, fossil fuels could meet the growing energy demand during this century [1], however, this would contribute to a large increase of CO_2 emissions which are already considered as too high. These emissions are believed to be the main cause of global warming [2]. The main, renewable, alternatives for fossil fuels are electricity (from for example solar panels), hydrogen and biomass. Electricity however is very difficult to store, while hydrogen requires large scale changes in energy infrastructure (for mobile use), making them at best a long term solution. Biomass can not meet the energy demands at all [3].

Large portions of the world energy demand are used for transportation in the form of liquid fuels like diesel or gasoline. The problem with replacing fossil fuels by any one of these alternatives is that they have a much smaller energy density [3], which would mean that for transportation, larger volumes and mass would have to be carried along.

Another alternative has emerged which combines the advantages of fossil fuels while also being sustainable. This alternative is based on the idea of extracting CO_2 from the atmosphere or collecting it on-site and synthesizing it into liquid, renewable and sustainable hydrocarbon fuels. In doing so, energy from renewable sources (solar, wind or water energy for example) is effectively stored in the chemical bonds of the hydrocarbons. This offers the possibility of using electricity, for example from renewable solar or wind energy sources [4] to convert CO_2 into high energy density (mobile) fuels which can be distributed using existing infrastructure for liquid fuels.

This conversion is already done by nature itself in the photosynthesis process, which converts CO_2 and water into glucose $C_6H_{12}O_6$ using sunlight. However, the highest reported energy efficiency for artificial photocatalytic conversion of CO_2 into hydrocarbons is only 0.0148% [5], making it commercialy unfeasible. The process limiting step in this conversion is the dissociation of CO_2 into CO. To improve efficiency, a plasma can be used to dissociate the CO_2, where energy efficiencies of up to 80% have been reported [6]. In this experiment, a Dielectric Barrier Discharge (DBD) in a flow tube reactor is used as a non-equilibrium plasma source. The highest reported energy efficiencies for a DBD are around 30% [7]. The advantage of the DBD is that it can be sustained at atmospheric pressure, making pumps only necessary to achieve flow and not for maintaining low pressures. Another advantage of the DBD is that it can easily be scaled up to industrial capacity [8].

In the conversion process of CO_2 into CO, it is important to know which species are created and in what quantities, to be able to optimize the conversion efficiency. The used DBD was already partly characterized before, where CO and O_3 mixing ratios were measured using ex-situ Fourier Transform InfraRed (FTIR) spectroscopy. However, molecular oxygen is also created in the plasma, which was not directly measured before. Therefore, this experiment will focus on how to measure the molecular oxygen mixing ratios and these will be cross checked against oxygen mixing ratios that were estimated from the oxygen balance and FTIR spectroscopy measurements.

2. Theory

2.1. Dielectric barrier discharge

A Dielectric Barrier Discharge (DBD) is a discharge occuring between two electrodes, which are (partly) covered by dielectric material and seperated by a gap (some possible configurations are shown in Figure 2.1). There can only be a current across the gap when a voltage is applied, which generates an electric field in the gap. Once this electric field exceeds the breakdown barrier of the gas, microdischarges can be observed in the gap between the dielectrics.

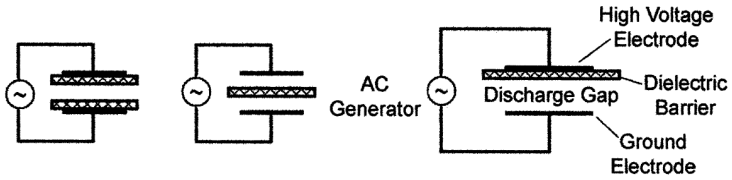

Figure 2.1.: Different possible types of DBD configurations. The first (symmetric) type is used in the experiments described in this report, having dual dielectrics at both electrodes. It is also possible to only use a single dielectric, resulting in either the second or third (asymmetric) configuration. [8]

The observed microdischarges occur because the electric field in the gap accelerates electrons in the gas. These accelerated electrons can ionize gas species, therefore producing more electrons. When the amount of accelerated electrons is high enough, a streamer is created (Figure 2.2). This streamer is a temporary 'channel' through which current can flow across the gap, creating a plasma [9]. The negative charges that are transported across the gap result in a buildup of negative charge in the dielectric. After a few nanoseconds they will neutralize the initial electric field and thus terminating the streamer [10].

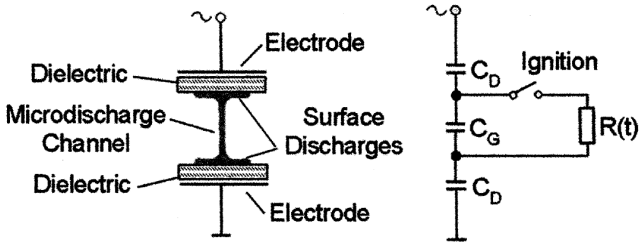

Figure 2.2.: A schematic representation of a microdischarge in a DBD and its equivalent electrical circuit [8].

The electrons transported to the dielectric will not move without an external electric field, which explains why a DC current cannot sustain a plasma. However, when an AC current is applied, the buildup of electrons in the dielectric can help the creation of streamers in the opposite direction.

2.2. Molecular energy levels

The energy states of molecules are, like atoms, discrete. This also means that transitions can only have discrete energy differences $\Delta E = E_2 - E_1$ where E_2 and E_1 are the energies corresponding to discrete energy levels of the molecule. Unlike an atom however, a molecule does not only have electronic transitions, but also stores energy in rotational and vibrational states. The energy differences attributed to the rotational states are significantly smaller then the energy differences attributed to vibrational states, which are in its turn, significantly smaller then the energy differences of electronic transitions.

Transitions between energy levels can either emit a photon when the energy difference is negative, or absorb a photon when the energy difference is positive. The difference between energy levels is directly related to the energy of the photon and thus its wavelength by:

$$\Delta E = E_2 - E_1 = \hbar\omega = \frac{2\pi\hbar c}{\lambda} \tag{2.1}$$

Each molecule has different energy levels and therefore different transitions between them. Larger, more complex, molecules for example, have a larger moment of inertia, its rotational energy levels are closely spaced, resulting in overlapping spectral lines. In the mid infrared, absorption lines are attributed to these rotational transitions. Therefore, instead of individual lines, a band of absorption will be seen. This occurs for example for ozone, but not for the simpler carbonmonoxide. Both are shown Figure 3.4. These energy level spacings provide a unique 'fingerprint' for each molecule by means of its absorption or emission spectrum.

2.3. Absorption spectroscopy

Absorption spectroscopy is used to determine the composition of an unknown mixture of species by its electromagnetic spectrum. The basic principle is that light travels through a collection of species. These atoms will absorb light with wavelengths corresponding to the differences between energy levels in the atoms, thus exciting electrons to higher states. The relation between the concentration of atoms, the effective absorption path length and the amount of light absorbed is given by the Beer-Lambert law.

2.3.1. Beer-Lambert law

The change in electromagnetic radiation for a thin slab with height dz is proportional to the intensity of the incident light $I(\nu)$, the height dz and some absorption coefficient $k(\nu)$. The assumption is made that only absorption occurs, while emission is absent. This leads to the differential equation for a thin slab:

$$dI(\nu) = -k(\nu)I(\nu)dz \tag{2.2}$$

.

Here $k(\nu)$ is the total absorption coefficient, which is a combination of absorption coefficients belonging to different species. A species i has its own absorption coefficients $k_i(\nu)$. The total absorption coefficient $k(\nu)$ is now defined as:

$$k(\nu) = \sum_i k_i(\nu) = \sum_i n_i\sigma_i(\nu) \tag{2.3}$$

where $\sigma_i(\nu)$ is the absorption cross section of species i and n_i the number density of this species. Throughout this report, not only the number density is used, but also the mixing ratio, which is defined as n_j/n_0 where n_0 is the total amount of particles in a specified volume. n_0 can be calculated using the ideal gas law:

$$n_0 = \frac{p}{k_B T} \tag{2.4}$$

where p is the pressure in Pascal, k_B is the Boltzmann constant and T is the temperature in Kelvin. This mixing ratio is often expressed in parts per million (ppm) or parts per billion (ppb).

Solving the differential equation 2.2 by splitting variables and integrating over a given path-length L through a homogeneous medium (i.e. constant pressure, temperature and absorption coefficient) gives an equation for the intensity of the signal:

$$I(\nu) = I_0(\nu) \exp^{-k(\nu)L} \tag{2.5}$$

This is known as the Beer-Lambert law. Rewriting this slightly gives a more convenient equation:

$$A(\nu) = \ln\left(\frac{I_0(\nu)}{I(\nu)}\right) = k(\nu)L \tag{2.6}$$

where A is known as the absorbance. The quantity $\frac{I(\nu)}{I_0(\nu)}$ is known as the transmittance. Integrating $k(\nu)$ over a single absorption line gives the integrated absorption coefficient K:

$$K = \int_{-\infty}^{\infty} k(\nu)d\nu = \frac{1}{L}\int_{-\infty}^{\infty} A(\nu) \tag{2.7}$$

For a single line due to species j, the line strength relates the absorption cross section $\sigma_j(\nu - \nu_0)$ centered at ν_0 to a normalised line profile $\phi(\nu - \nu_0)$ centered at ν_0 by the equation:

$$\sigma_j(\nu - \nu_0) = S(T)\phi(\nu - \nu_0) \qquad \int_{-\infty}^{\infty} \phi(\nu - \nu_0)d\nu = 1 \tag{2.8}$$

If this line is due to species j, the integration over $k(\nu)$ reduces to an integration over $k_j(\nu) = n_j\sigma_j(\nu)$ giving:

$$K = \int_{-\infty}^{\infty} n_j S(T)\phi(\nu)d\nu = \frac{1}{L}\int_{-\infty}^{\infty} A(\nu) = nS(T) \tag{2.9}$$

where n is the number density, and $S(T)$ is the line strength. As is evident from Equation 2.9, the integrated absorption coefficient is proportional to the number density and a proportionality factor $S(T)$. The shape of the absorption line however has not been defined using any of the previous equations.

2.3.2. Line profiles

The shape, or profile of an absorption line $\phi(\nu - \nu_0)$ is caused by multiple line broadening effects. The most important broadening types for these studies will be discussed below. To quantify these, the half width at half maximum (HWHM, or also known as spectral width) is often used. The HWHM is the distance in wavenumbers between the point where the line profile has its maximum value and the point where the line profile has a value of half the maximum value.

Natural broadening

The energy level of an excited state is limited by the uncertainity principle. This directly states that the uncertainty in energy is never zero, and thus that the absorbed wavelength is not a single value but rather a (Lorentzian) distribution of wavelengths. This causes a broadening of the absorption lines. The following equations describe the natural broadening:

$$\Delta E \Delta t \approx \hbar \qquad \Delta\nu_{nat} = \frac{\Delta E}{hc} \qquad \Delta\nu_{nat} \approx \frac{1}{2\pi c\tau} \tag{2.10}$$

where ν_{nat} is the natural broadening half width in cm^{-1} and τ is the lifetime of an exited state. This lifetime is for example for ro-vibrational transitions typically between 10^{-3}s and 1s, which results in a typical natural broadening half width of $10^{-10} - 10^{-7}$ cm^{-1}. Normally, the natural broadening effect is negligible compared to collision- and Doppler broadening.

Collision broadening

Collision broadening (also known as pressure broadening) is caused by the collision of excited species, thus reducing their lifetime and increasing the uncertainty of the energy levels, which broadens the spectral line. This broadening gives a Lorentzian line profile, described by:

$$\phi(\nu - \nu_0) = \frac{1}{\pi} \frac{\Delta\nu_{col}}{(\nu - \nu_0)^2 + \Delta\nu_{col}^2} \tag{2.11}$$

where the halfwidth $\Delta\nu_{col}$ in cm^{-1} is proportional to the number of collisions per unit time:

$$\Delta\nu_{col} \sim \frac{p}{T}(kT/m)^{1/2} \sim \frac{p}{T^{1/2}} \tag{2.12}$$

where p is the pressure in Pascal and T is the temperature in Kelvin.

Doppler broadening

Doppler broadening is caused by the movement of molecules in the absorption path. When molecules move towards the source of the light, the wavelength of the incident light is reduced, known as the Doppler effect. The inverse effect happens when a molecule moves away from the light source. Doppler broadening results in a Gaussian line profile:

$$\phi(\nu - \nu_0) = \frac{1}{\alpha_D\sqrt{\pi}} \exp\left(-\frac{(\nu-\nu_0)^2}{\alpha_D^2}\right) \qquad \alpha_D = \nu_0\sqrt{\frac{2k_BT}{mc^2}} \tag{2.13}$$

where m is the mass of a single molecule. For a Gaussian line profile of this form, the halfwidth at half max is $\alpha_D\sqrt{\ln 2}$, resulting in:

$$\Delta\nu_D = \nu_0\sqrt{\frac{2k_BT\ln 2}{mc^2}} \tag{2.14}$$

Given these equations for the spectral widths, it is now possible to approximate the integrated absorption coefficient for the case where Doppler broadening is dominant (low pressures). In that case, we can assume the line profile to be Gaussian, thus giving an approximation for the integral in Equation 2.7:

$$K = \frac{1}{L}\sqrt{\frac{\pi}{\ln 2}} \ln\left(\frac{I_0(\nu_0)}{I(\nu_0)}\right) \Delta\nu_D \tag{2.15}$$

where ν_0 is the center wavenumber of the absorption line. The same can be done for relatively high pressures (>100mbar), where the line profile can be assumed to be Lorentzian, thus yielding a value for the integrated absorption coefficient:

$$K = \frac{\pi}{L} \ln\left(\frac{I_0(\nu_0)}{I(\nu_0)}\right) \Delta\nu_{col} \tag{2.16}$$

2.4. HITRAN database

The HIgh resolution TRANsmission database (HITRAN) contains molecular spectroscopic parameters for (mainly infrared) absorption lines of 42 molecules [11] (in the 2008 version). These line parameters include: wavenumber in cm^{-1}, line strength in cm molecule^{-1} at 296K, the air-broadening, or pressure broadening coefficient (HWHM) in cm^{-1}/atm at 296K, a coefficient of temperature dependence of air-broadened halfwidth and others [12, 13].

These parameters can be used to calculate the line profile of various lines in the HITRAN database. An example is given in Figure 2.3 for molecular oxygen lines in the A-band ($b^1\Sigma_g^+ \leftarrow X^3\Sigma_g^-$) around 763nm (where the laser will emit) in 1m of room air. The HITRAN database usually only contains ro-vibrational transitions in the (mid-)infrared range. Molecular oxygen is a exception, but is included because it is well studied for remote sensing applications in the atmosphere.

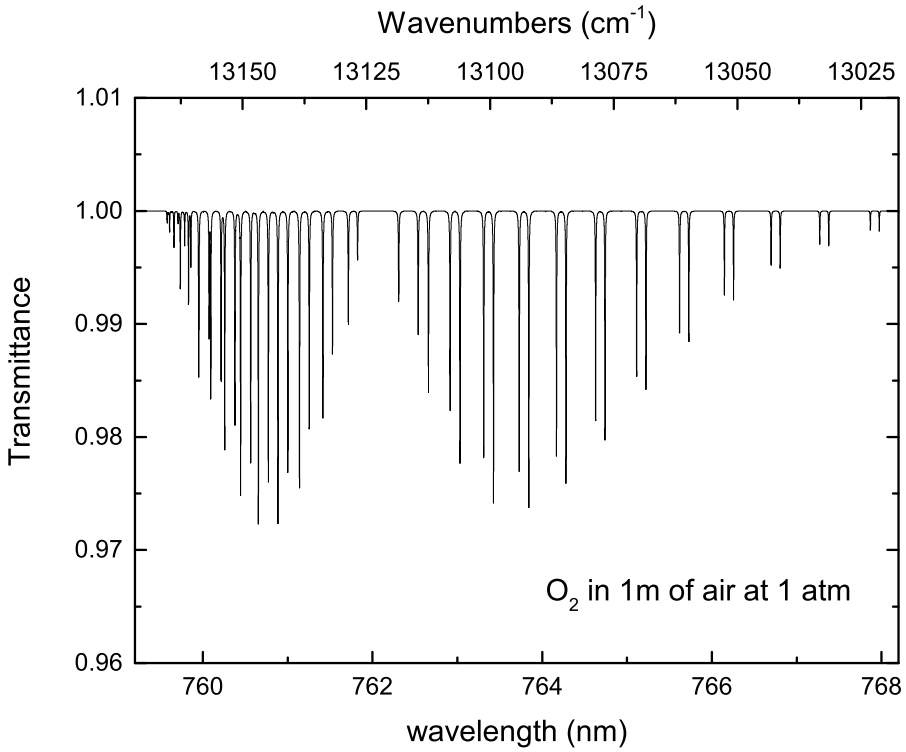

Figure 2.3.: The transmittance graph for oxygen in room air at atmospheric pressure around 763nm.

3. Experimental setup

3.1. Overview

A schematic overview of the setup is given in Figure 3.1. In the setup, a Mass Flow Controller (Bronkhorst, El-Flow F-201C) regulates the amount of pure carbondioxide gas injected into a dielectric barrier discharge (see also section 3.2). The gas is pumped by a rotary vane pump in conjunction with a regulating valve to adjust the pumping speed and thus control the total pressure and residence time. The DBD is resonantly powered by a sinusoidal voltage. The voltage and current are measured and used to calculate the power consumption (and specific energy) of the discharge. In the DBD, carbondioxide is dissociated into (presumably) carbonmonoxide, molecular oxygen and ozone. This gas mixture is measured downstream in a Heriott type [14, 15] multipass cell and a single pass absorption cell aligned to a Fourier Transform IR (FTIR) spectrometer.

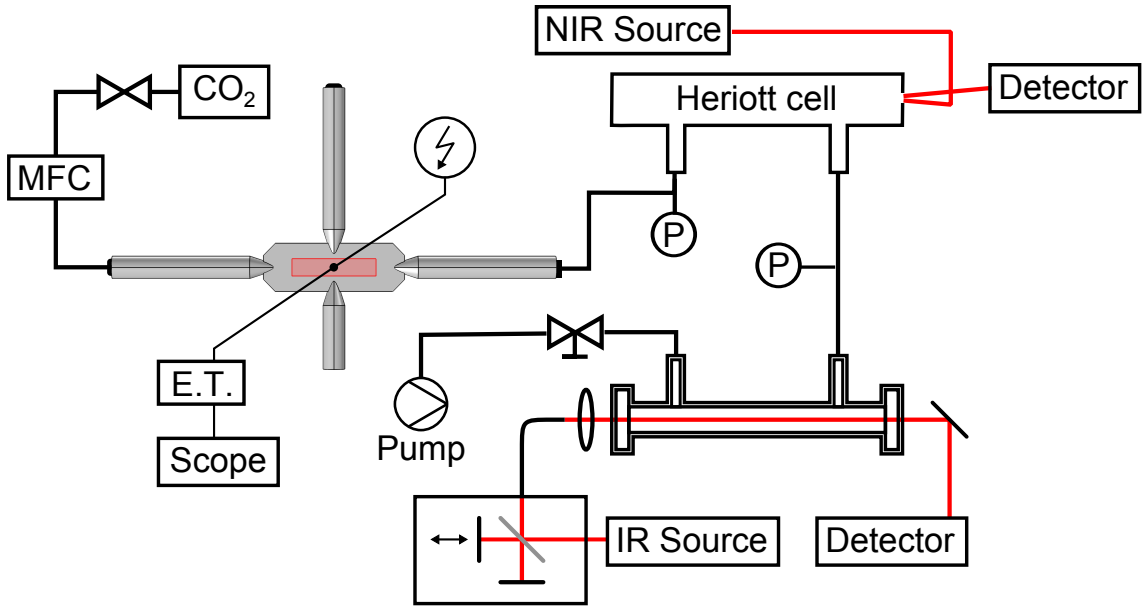

Figure 3.1.: A schematic general overview of the experimental setup.

In the Heriott cell (Aerodyne Research, Inc. - Astigmatic Multipass Absorption Cell, AMAC-LW-76), absorption spectroscopy is used to measure the mixing ratio of molecular oxygen. This part of the setup is schematically depicted in Figure 3.2. The Heriott cell extends the optical path length where absorption occurs to 76 meters, thus making it possible to measure relatively low concentrations of molecular oxygen. The light source used to perform absorption spectroscopy is an external cavity tunable diode laser (discussed in section 3.4), of which both the piëzo voltage and the current are modulated. The piëzo voltage is modulated to be able to scan a wavelength range, and is directly generated by the used software. The current modulation is necessary to introduce a 'signal off' period. The current modulation is generated by the delay generator (see also section 3.6) which is triggered on a custom signal from the software indicating the laser off period. This is especially important to determine the dark signal of the detector.

To fulfill the so-called re-entrant condition of the Heriott cell, the incident laser light requires a specific angle of indidence. Additionally, the laser beam has to have a specific focal length upon entry of the cell. To transform the laser beam to the required beam shape, several optics elements where used (section 3.4). Focussing the laser beam was achieved by a commercially available optics board. However, this board was designed for a highly divergent light source. Therefore, an additional lens was used to focus the laser beam to the (imaginary) position of the light source for which the optics board was designed.

A bandpass filter is placed just after the laser, which blocks light that does not have a wavelength close to 764nm. After this filter, a series of 3 flat mirrors is placed. One of these three mirrors is used to change the height of the optical path relative to the optics board, and is therefore not included in figure 3.2. The other two mirrors are used to easily adjust the optical path in the plane parallel to the optics board. The first elliptical mirror focusses the light on the matching point of the two focii of the elliptical mirrors. The second elliptical mirror then focusses the beam on the correct point inside the cell (as specified by its manual). When the light exits the cell, it is guided towards the detector (ThorLabs DET10A/M) and focussed on the detection element by a lens of short focal length. This light is then recorded by the detector and processed by the software (described in section 3.7).

The gas mixture exiting the Heriott cell flows into a single pass absorption cell where FTIR spectroscopy (described in section 3.3) is used to measure mixing ratios of both (infrared active products) carbonmonoxide and ozone. This provides a means of estimating the oxygen mixing ratio measured in the Heriott cell by calculating the oxygen balance of the stable species.

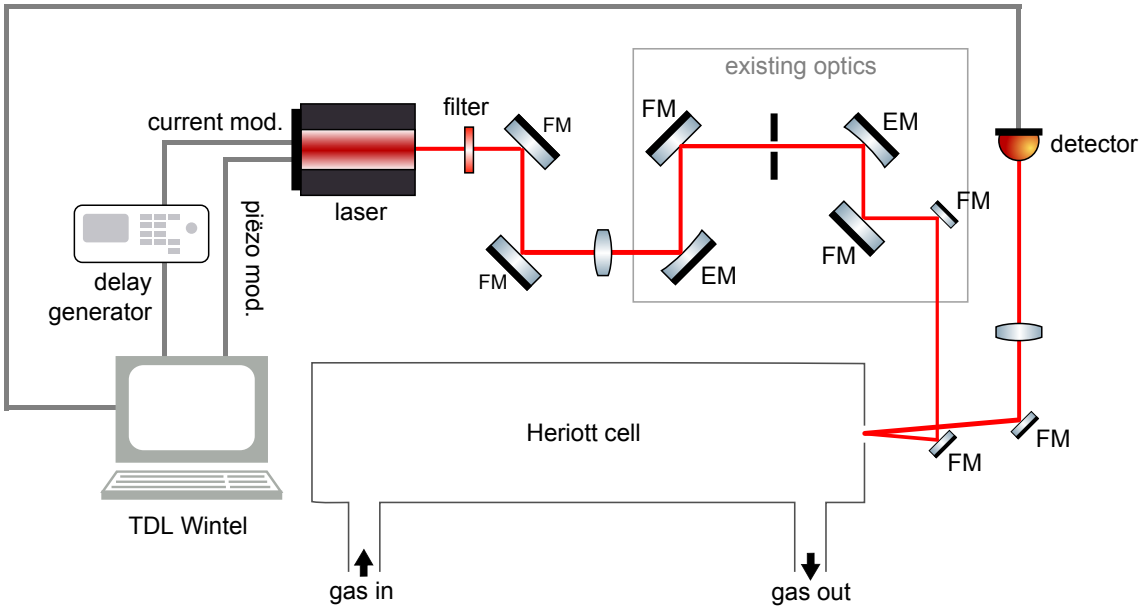

Figure 3.2.: A schematic overview of the experimental setup for measuring the oxygen mixing ratio in the Heriott cell. FM stands for flat mirror, while EM means elliptical mirror

3.2. Dielectric barrier discharge

A quartz glass flow tube is used as the plasma reactor. The flow tube consists of two parallel plates spanning the active region of the DBD, connected to two quartz tubes for gas injection and exhaust. This quartz glass serves as a discharge container, but also as the dielectric necessary for the DBD. Onto this quartz glass, flat electrodes with round ends are glued. These electrodes have a length of 70mm and a width of 16mm. The gap between the dielectric material is either 1mm or 3mm. Two DBD reactors were used, for which the specifications are listed in table 3.1.

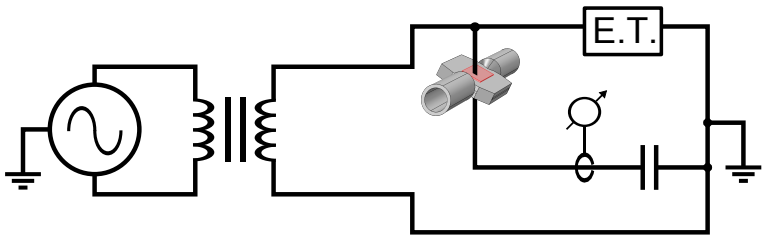

Figure 3.3.: The electronics used to power the DBD and to analyse the applied voltage and discharge currents.

The electronic circuit is depicted in Figure 3.3. A transformer is used to excite the plasma. A sinusoidal voltage with a frequency of about 60kHz and an actively controlled amplitude is applied. It is possible to pulse this voltage, where the on-period and off-period can be set in milliseconds, resulting in an on-period containing tens up to hundreds of individual AC cycles. A convenient unit to express the ratio between on- and off-period is the duty cycle, defined as:

$$d.c. = \frac{t_{on}}{t_{on} + t_{off}} \tag{3.1}$$

where t_{on} is the on-period in seconds and t_{off} is the off-period in seconds. The voltage applied to the reactor is converted from high voltage to lower voltages by a custom-made voltage divider and is then measured. The discharge current is measured directly using a current transformer. The current is also measured indirectly by measuring the charge on a capacitor. All these signals are captured by a fast digital oscilloscope (LeCroy, WaveRunner 610Zi). The temperature of the reactor is monitored using an IR camera (FLIR A320).

	Gap size	Dielectic thickness	Pressure	Flow rate	Residence time
Tube A	1.0mm	1.5mm	100-1000mbar	135-1700sccm	25-775ms
Tube B	3.0mm	1.0mm	100-1000mbar	150-1550sccm	100-1500ms

Table 3.1.: A listing of the specifications of the tubes used in this experiment.

3.3. Fourier transform infrared spectroscopy

The stable species present in the gas mixture produced by the dielectric barrier discharge are carbondioxide, carbonmonoxide, molecular oxygen and ozone. The mixing ratios of the infrared-active molecules like carbonmonoxide and ozone can be measured using Fourier Transform InfraRed (FTIR) spectroscopy. The setup for this is custom built, where the gaseous sample flows through a 49cm long stainless steel tube with 2 KBr windows. This tube is aligned to a commercial FTIR device (Bruker, IFS 66/S) via an IR fibre. First,

a baseline is measured without the discharge being active. Then, the discharge is started, resulting in another spectrum. From these spectra, the transmittance is calculated, of which an example is given in Figure 3.4, where the carbonmonoxide and ozone absorptions can be clearly seen. The mixing ratio of carbondioxide is not measured using FTIR spectroscopy, because it is very difficult to substract the environmental contribution of CO_2.

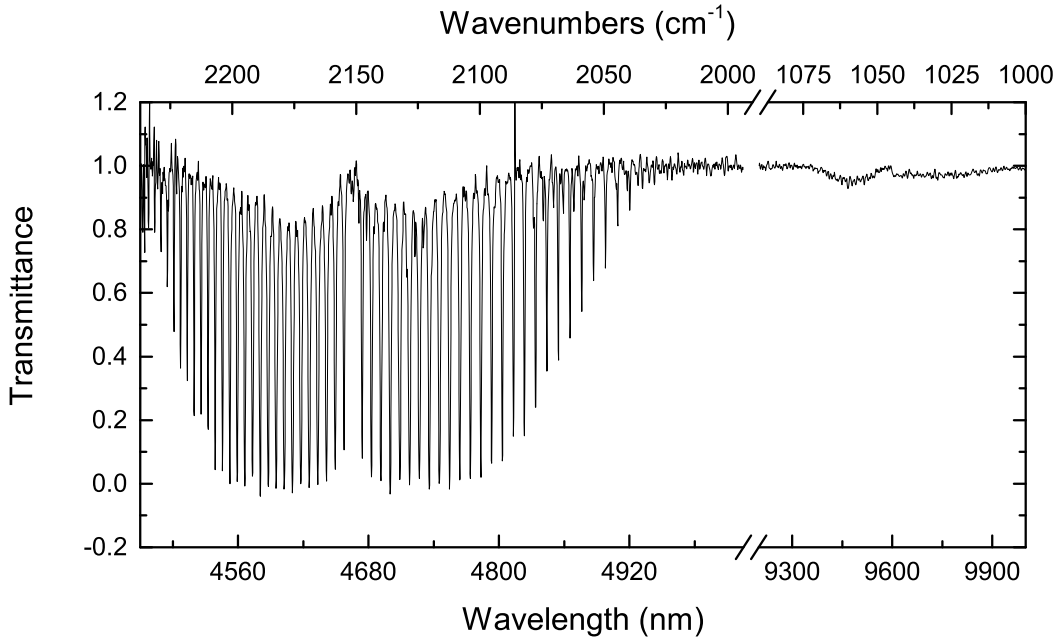

Figure 3.4.: The transmittance of a gaseous sample from the exhaust of the plasma after correction for the plasma-off contributions. This sample contains carbonmonoxide and ozone, which are measured using an FTIR spectroscopy. The absorption due to carbonmonoxide is visible between 4500nm and 4900nm, while the absorption between 9300nm and 9900nm is due to ozone molecules. Note that the mixing ratio is CO is high enough to generate a saturated transmittance spectrum, which would be difficult for analysis.

These absorption lines for carbonmonoxide and ozone can be compared with line profiles generated by a program like Q-MACSoft-HT (neoplas control GmbH), which generates an absorption spectrum for a given pressure, mixing ratio, temperature, instrumental broadening and path length (for this FTIR device 49cm). The program uses parameters from the HITRAN database to generate an absorption spectrum. The analysis of the FTIR spectroscopy measurements are very time consuming. Therefore, a script was written to automate this. This script can calculate the mixing ratio in parts per billion from a given FTIR spectrum and a given reference measurement generated by the Q-MACSoft-HT tool. How this is implemented in detail is discussed in Appendix B.

3.4. Laser

The laser used is an EOSI LCU-2010-M with a laser diode module of the type DMD770-010 produced by Newport Corp. The grating used in the external cavity of the laser is the GRAT-1800 which is designed for a wavelength range between 621nm and 880nm. The laser diode has a center wavelength of 770nm according to its specifications. However, the laser diode emits significantly more towards 780nm then towards 760nm, as can be seen in Figure 3.5.

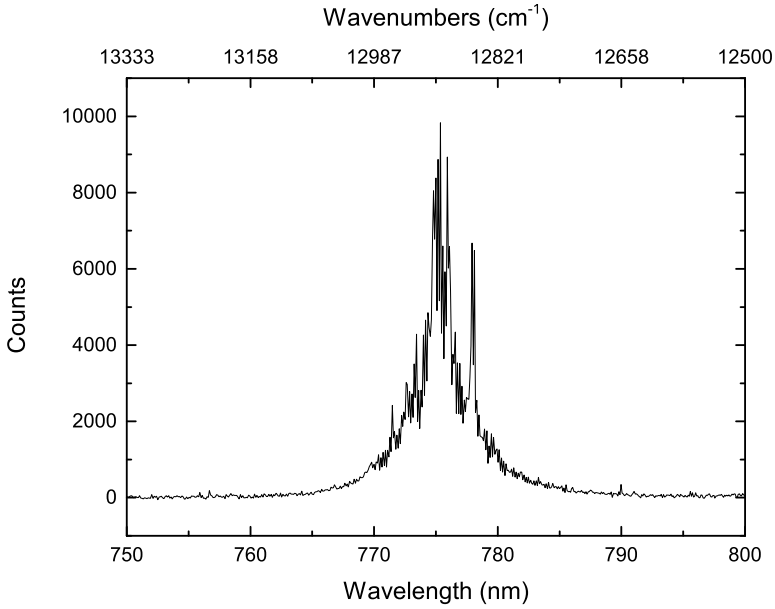

Figure 3.5.: The spectrum of the laser diode module (DMD770-010)

The emission spectrum of the laser diode defines a lower wavelength limit below which the emission is almost negligible. However, as Figure 2.3 shows, the position of the absorption lines of oxygen give an upper limit for the wavelength used for measurements. Therefore, the goal is to search for a wavelength where the amount of signal on the detector is still acceptable (restricted by the laser diode), while around the wavelength used there are still significant absorption lines. In practise, the laser cannot emit below 763nm, which would suggest that a wavelength around 764nm should be used for maximum absorption. Because 764nm is so close to the lower operation limit of the laser, this in practise means that mode hops are quite common.

Because of these limitations, the absorption line pair at wavelengths 764.17nm (13086.13 cm^{-1}) and 764.28nm (13084.20 cm^{-1}) is used for measurements. At these wavenumbers, the laser emits without modehops, while the absorption is still relatively high for these lines. For this choice of wavelength, the emission spectrum of the laser is shown in Figure 3.6.

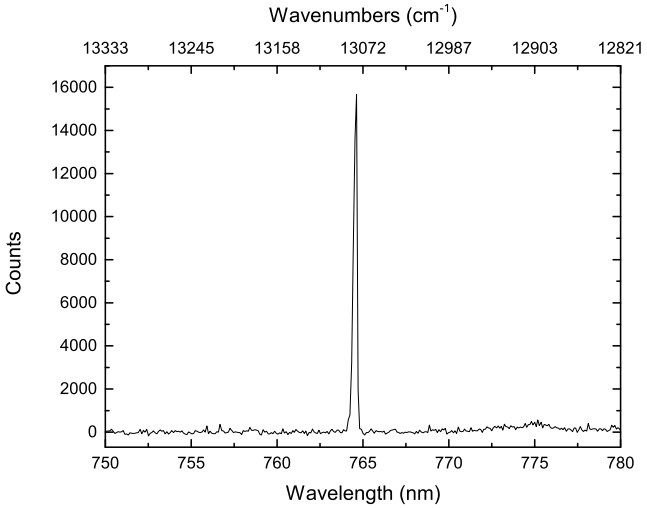

Figure 3.6.: The unfiltered emission spectrum of the laser with an emission peak at 764.2nm

3.5. Bandpass filter

As Figure 3.6 shows, the laser does not only emit at the desired wavelength of 764nm, but it also emits around 775nm, though with a relatively low intensity. This light will not be absorbed by any oxygen and will therefore give an undesired offset in the absorption spectrum, which results in inaccurate data. This is especially a problem when the laser is scanned over a wavelength range, because this unwanted emission does not have a constant intensity during the wavelength scan. For this reason, a filter (Thor Labs FB760-10 bandpass filter) is introduced to block this emission, which results in the emission spectrum shown in Figure 3.7.

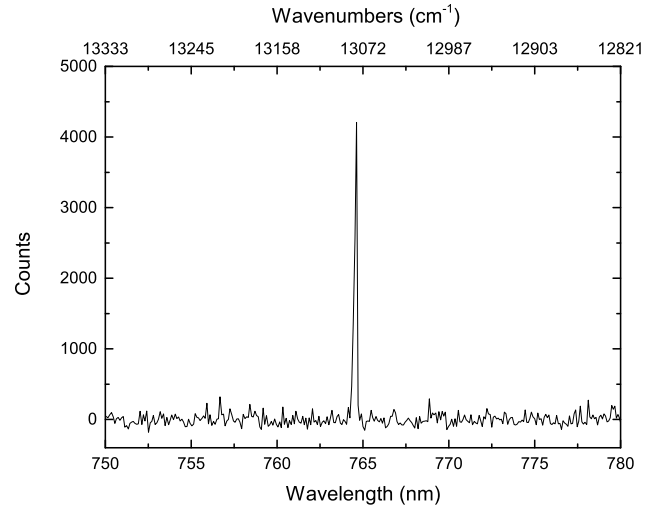

Figure 3.7.: The filtered emission spectrum of the laser with an emission peak at 764.2nm

3.6. Delay generator

Normally, the software would be used to generate a voltage ramp for modulating the current. Because in this experiment, modulation will occur by means of modulating the piëzo, a second signal needs to be generated for the current modulation to shut the laser off every measuring

period. This 'laser off' period is needed by the software to record the zero signal of the detector. The software used is however not designed for a doubly modulated laser. Usually, only current modulation is used for both the scanning of the laser over a wavelength range and generating the laser off period.

For the laser diode used in this experiment, the laser stops emitting below a current of 80mA. For maximum laser intensity, a current of 125mA is applied. Considering the gain of the laser of -10mA/V, a voltage of +4.5V is needed to stop the laser emitting. To achieve this, the software generates a short pulse on a second output channel, after which there is a period in which both the piëzo and current modulation are zero. A delay generator is then used to apply the desired voltage to suppress the laser during the desired off-period.

3.7. Software

TDL Wintel, developed by Aerodyne Research Inc., is used as a software to sweep the laser across the chosen oxygen absorption line pair and to record and analyse the absorption spectra. This software is able to generate a voltage ramp for the piëzo modulation by means of a National Instruments Data Acquisition (DAQ) Card. The software also generates a trigger signal for the 'laser off' period, which is fed to the delay generator. The detector is also connected to the DAQ card, so that the software can display and analyse this signal.

3.7.1. Auto background

Because of the way the experiment is set up, there is an absorption path even before the light enters the cell, with about 21% oxygen, which will absorb some of the signal already. Because this can significantly influence the mixing ratios, the software first measures a background spectrum with the cell pumped down to base pressure and divides every spectrum it measures by that background spectrum, therefore eliminating the absorption before entering (and also after exiting) the cell.

3.7.2. Fitting

The software is able to fit the absorption lines, and from that directly retrieve the mixing ratio of different species. This requires that the software is given values for the pressure (in this case measured by a pressure gauge and connected to the DAQ card), temperature, optical path length and the wavenumbers of the pair of lines that are being fit, including a reference to a HITRAN database file containing spectral data about the measured absorption lines. Note that the temperature in the absorption cell is constant, since the gas temperature is reduced to room temperature already before entering the cell. Also, a relative wavenumber calibration is done using a 11.9mm long BK7 etalon. The software can fit the fringes created by this etalon and do the relative wavelength calibration from this. This actual analysis of the mixing ratios is done by fitting the baseline with a polynomial of up to sixth order, and fitting the absorption lines with a Voigt profile. Because the laser sweeps over an absorption line pair, it is therefore possible to fit the two lines seperately and thus gaining two different mixing ratios, which should in theory be the same.

4. Results and discussion

Before any results will be discussed, the system will be characterized in section 4.1. This includes the calculation of the error margins, calibration measurements and some simplification of the results is done. After this, the experimental results will be discussed for both direct measurement and estimates using the oxygen balance in section 4.2, followed by a comparison of the two different plasma reactors in section 4.3.

4.1. System behaviour

For the calculation of the mixing ratios, the correct line parameters have to be provided. For this reason it is vital to know exactly which lines are detected. Unfortunately, the laser can only scan the range of two absorption lines. Because an absorption line pair is not very distinctive from its neighbouring pairs, a calibration measurement is done in room air at 1000mbar to find the absolute wavenumbers of each absorption line pair. Equation 2.16 shows that at high pressures the absorbance value at the center of the absorption line is proportional to the line strength. Therefore, the peak value of the absorbance is measured as a function of the wavelength as displayed by the laser power supply and then compared to the linestrengths from the HITRAN database. This provides an offset value for the wavelength displayed by the power supply as a correction, so that identifying the desired absorption line pair is possible. The result of this measurement is shown in Figure 4.1

In order to scan over a wavelength range that includes two absorption lines in one sweep (an example is shown in Figure 4.2), the maximum tuning range of the piezo element has to be used. Unfortunately, this also increased the tendency of the laser to mode-hop. The software makes it possible to fit both of these lines using a single fit and thus resulting in a single mixing ratio. However, this fitting procedure is very sensitive to any change in distance between the two lines. Normally, this distance would not change, but because the laser is quite mode-hop sensitive, mode hops could occur during a measurement, thus affecting the fit. The alternative is to fit both lines seperately, which results in two mixing ratios for the molecular oxygen. This makes the mixing ratios less sensitive to mode hops. In this way, these mode hops will only affect the measurement when they occur at the position of an absorption line or very close to it.

Using this method, it is possible to verify whether the mixing ratios are correct, during measurements. There should not be a large difference in mixing ratios calculated by the software for both lines. If there is a large difference, this could be an indication of mode hopping. In Figure 4.3, a measurement series is given to indicate the difference between the two oxygen mixing ratios. Because there is little difference between the two mixing ratios, only one will be shown in figures from now on, while the other measurement is omitted. The average difference between the two mixing ratios (660ppm), which is mainly a systematic error, will be doubled and used as the uncertainty (e.g. 1320 ppm). It is important to note that the difference between the two measured mixing ratios is not constant, but depends on the specific energy, therefore overestimating the uncertainty for small specific energies whilst underestimating the uncertainty for high specific energies. The uncertainty of 1320ppm is mainly due to a curvature in the baseline of the measurements as a result of slight mechanical

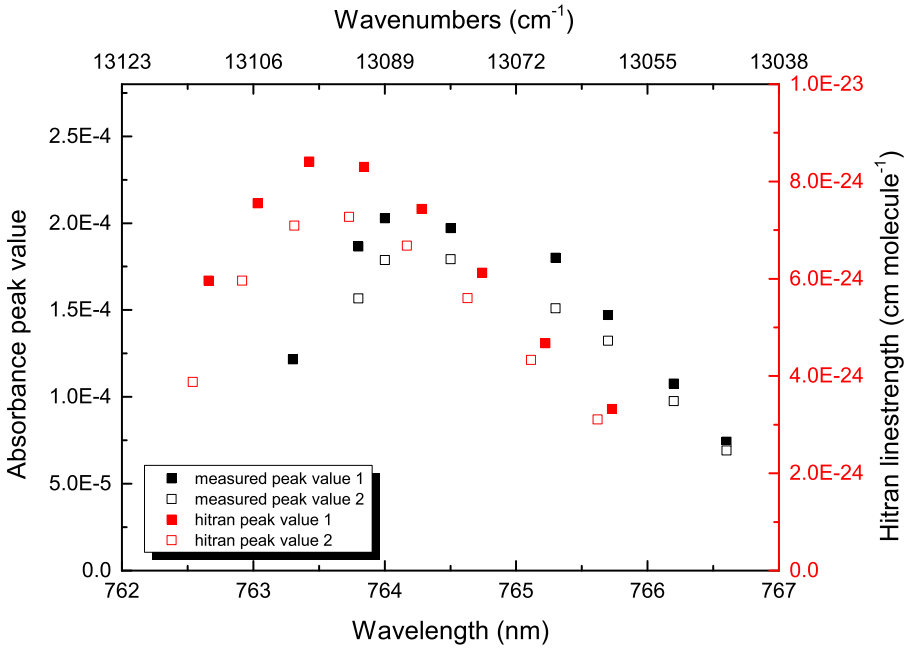

Figure 4.1.: The linestrengths in red from the HITRAN database as function of wavelength. In black, the absorbance peak value as a function of wavelength (as indicated by the laser power supply). From these data points, the offset in real wavelength and the wavelength provided by the laser power supply can be determined. The black data points are not spaced evenly as would be expected, however this is because the wavelength reading on the power supply is fluctuating as a result of the scanning over a wavelength range. The same is true for the wavenumbers on the top axis, since they are calculated from the wavelength given by the power supply. These wavelengths however, are accurate enough to distinguish the line pairs from each other.

fluctuations in the laser diode. This curvature results in a slight overestimation of one mixing ratio while the other is slightly underestimated.

Apart from the uncertainty introduced by only displaying one of the mixing ratios in the graph, there is also some intrinsic uncertainty in any oxygen mixing ratio measurement, which is a combination of uncertainties in multiple components in the setup, for example, the laser output power can vary slightly over time, mode hops can occur which changes the fitting process slightly, the pressure or temperature varies slightly over time etc. An estimate for this uncertainty is extracted from the Allan variance of the system [16, 17, 18]. For this, a measurement is done using room air at a constant pressure of 133 mbar inside the Heriott cell. The molecular oxygen mixing ratios were measured over the length of one hour. The Allan variance was then calculated and a double log plot was made, resulting in Figure 4.4.

From this, the intrinsic error of the entire spectoscopic system can be determined, which is the square root of the values displayed in Figure 4.4. From this, the error can be determine to be between 75ppm (for an integration time of 550 seconds) and 350ppm (for an integration time of 10 seconds), depending on how long one would integrate the mixing ratio provided by the software. For all plasma related measurements, an integration time between 2 and 10 seconds was used. Because this integration time was not well defined during measurements, the upper limit for the intrinsic uncertainty (350ppm) is used as uncertainty. Combining this with the systematic error of 1320ppm as argued from Figure 4.3, a total upper limit for

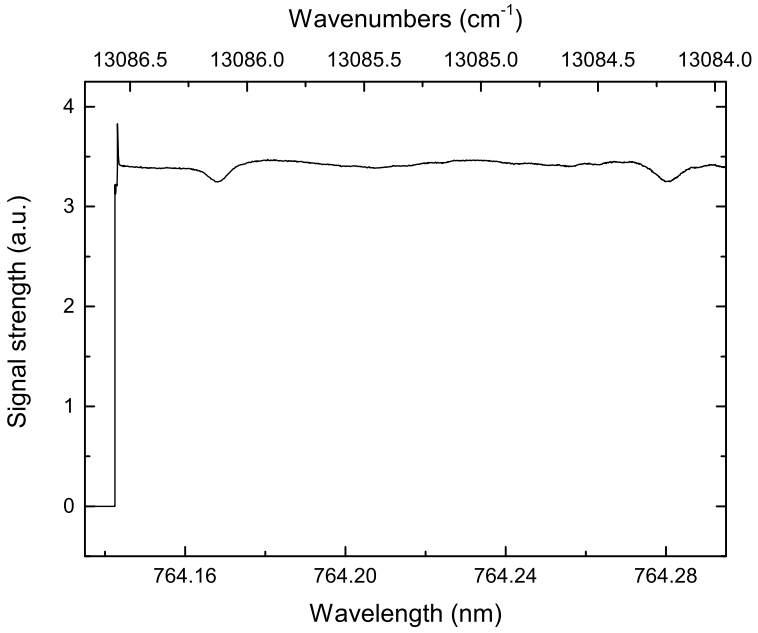

Figure 4.2.: The signal strength after baseline correction as function of wavelength. This absorption spectrum was recorded at a specific energy of 13.7 kJ/L, a flow of 234 sccm and at atmospheric pressure. Here, the plasma current was not pulsed. The off-period of the laser can also be seen at higher wavenumbers.

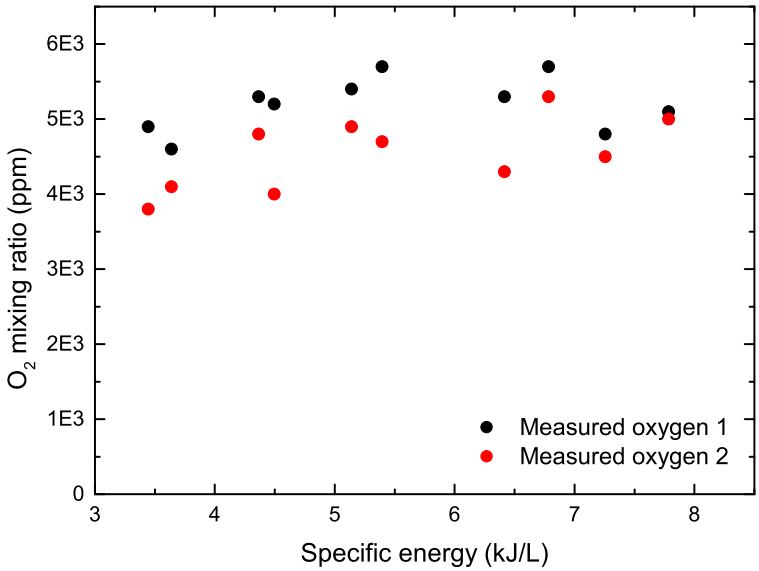

Figure 4.3.: The mixing ratio measured for both absorption lines as a function of the specific energy. These measurements are done with a constant flow of 450sccm on Tube B. The power and pressure were varied. This data gives an average difference in the two mixing ratios of $\sim$ 660ppm

the uncertainty is gained of 1670ppm.

For the FTIR measurements, the uncertainty can be estimated by checking what absorption line would not be distinguishable anymore from the noise on the FTIR signal, effectively using the limit of detection as an approximation for the uncertainty. The noise on the FTIR signal is about 4%, meaning that noise on a region without absorption lines spans between

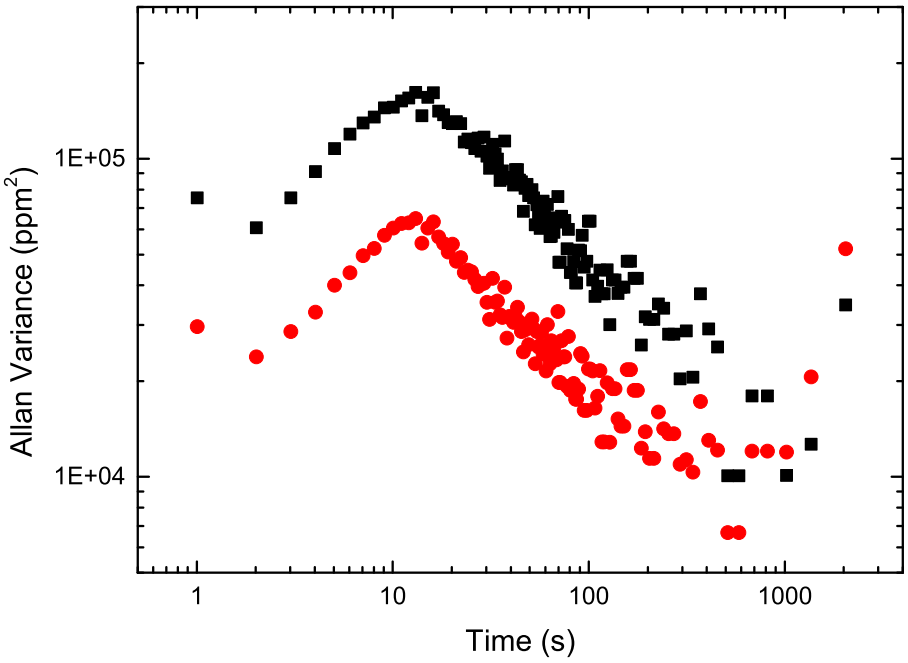

Figure 4.4.: The Allan variance of both mixing ratios (for both absorption lines) as a function of integration time in a double log plot. For this measurement, the mixing ratios of oxygen in room air were measured at a constant pressure of 133mbar over the course of an hour. Three regions can be distinguished: the positive slope between 2 and 10 seconds is attributed to atmospheric turbulence [16]. The second region, with negative slope, between 10 and 500 seconds, is due to white noise. The third region (>500s) is an increase again in the allan variance due to drift. The Allan minimum resides between the second and third region.

a transmission of 96% and 104%. This uncertainty is mainly determined by the accuracy of the baseline substraction. Since the transmission is affected by the mixing ratio of the species and the total pressure, the limit of detection is pressure dependent. Table 4.1 lists the mixing ratios at a given pressure that have, as a minimum, a transmission value of 96%. The limit of detection for O_2 is not estimated using the method above, but is calculated using the limits of detection for CO and O_3 and an uncertainty derivation of Equation 4.1.

Because the line strengths of CO and O_3 absorption lines are roughly a factor of a 1000 larger than the line strengths for the oxygen A-band, it is expected that the uncertainties in mixing ratios for CO and O_3 measured using FTIR spectroscopy will be smaller than for the TDLAS measurements.

Pressure (mbar)	CO limit of detection (ppm)	O_3 limit of detection (ppm)	O_2 limit of detection (ppm)
1000	16	33	58
800	19	40	70
500	28	60	104
300	45	95	165
200	65	140	243
100	130	280	485

Table 4.1.: Limit of detection for the mixing ratios of CO, O_2 and O_3 in parts per million for different pressures.

4.2. Oxygen balance and direct measurements

In this section, the results obtained from plasma measurements are presented and discussed. The plasma used is a pure CO_2 plasma created in a DBD reactor. Two different reactors were used for oxygen measurements. These are specified in Table 3.1. The main difference between the reactors is their volume to surface ratio, which may have some effect on the reactions in the reactor.

The oxygen mixing ratio in the exhaust of the plasma was determined in two different ways. First, the FTIR measurements were used to determine the CO and O_3 mixing ratios. From this, assuming that no other reaction products apart from CO, O_2 and O_3 are produced, a predicition can be given for the oxygen mixing ratio. Each CO_2 molecule dissociated into CO also produces one oxygen atom. These seperate atoms will react with each other, producing either O_2 or O_3. From this simple argument, an equation can be constructed to calculate the mixing ratio of O_2 produced by the plasma:

$$n(O_2) = \frac{1}{2}(n(CO) - 3n(O_3)) \tag{4.1}$$

where n is the number density of a specific species. Second, the oxygen mixing ratio is directly measured by using Tuning Diode Laser Absorption Spectroscopy (TDLAS), where the software can fit and analyse the absorption lines in real-time to give the oxygen mixing ratio in parts per billion.

Both methods were applied to a large variety of measurement series, where for example the pressure, flow, residence time or duty cycle were varied while other parameters were kept constant. From these measurement series, two will be used to illustrate the trend of the measurements. For any other measurement data, please refer to Appendix A. A more generalised discussion of the plasma chemistry is provided below.

Figure 4.5 shows a measurement series where atmospheric pressure was used with a constant duty cycle of 100%. This measurement was therefore not pulsed. The gas flow was varied between 148sccm and 1700sccm in order to systematically change the residence time. To get a spread of specific energies, the power was varied between 15 and 35 Watt for each value for the gas flow. From Figure 4.5, one can see that the trend of the measured oxygen mixing ratios is the same as for those ones that were predicted from the FTIR analysis. The difference between these increases slightly when higher specific energies are achieved. This is probably because at these conditions, the temperature of the reactor is usually higher, resulting in a lower O_3 mixing ratio. Because this mixing ratio is low, the signal to noise ratio of the O_3 absorption lines is smaller, resulting in a less accurate O_3 mixing ratio. Because the oxygen balance is heavily dependent on the amount of ozone produced, this would also result in a less accurate prediction for the oxygen mixing ratio.

In Figure 4.6, another graph is shown to illustrate that the results for the oxygen mixing ratio from the FTIR and direct measurements correspond very well. This measurement is pulsed, where the flow and power during the on-period of the plasma were kept constant. The pressure was varied, and for each pressure, four different duty cycles (e.g. 9%, 17%, 29% and 45%) were applied. From this figure, it is also clear that the general trend of both oxygen mixing ratio measurements is the same. Therefore, from here, only the directly measured oxygen mixing ratios using TDLAS are shown.

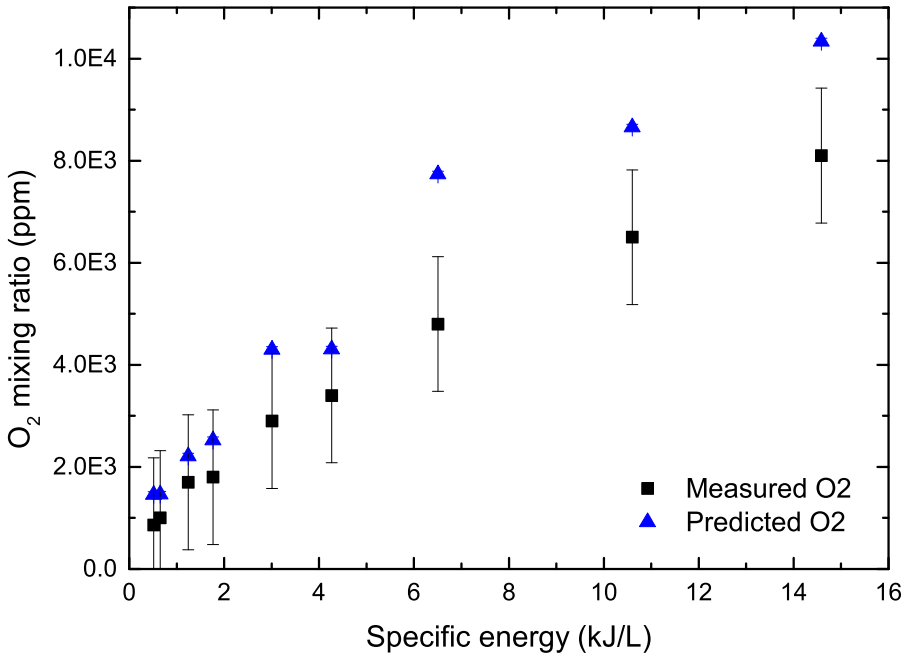

Figure 4.5.: The oxygen mixing ratio as function of the specific energy for measurements on Tube A using a constant pressure of 1000mbar, a duty cycle of 100% and a gas flow varying between 148sccm and 1700sccm. For each flow used, measurements were performed for three differents powers to get a spread in the specific energy.

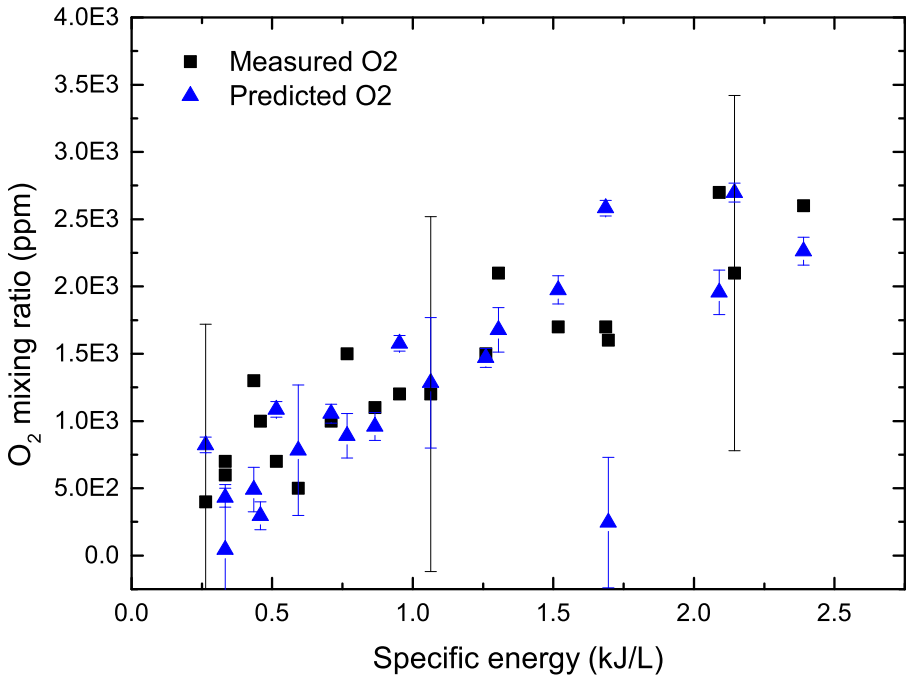

Figure 4.6.: The oxygen mixing ratio as function of the specific energy for measurements on Tube A using a constant flow of 518sccm. The power during the plasma on-period was kept constant, while the pressure was varied. For each pressure, the oxygen mixing ratios were measured for four different duty cycles. Errors bars are only included for some measurements.

4.3. Oxygen production in different plasma reactors

To study the plasma chemistry and generalise the discussion it is useful to combine the results of individual measurement series to study the process parameters that are of importance to the oxygen mixing ratio. The individual measurements can be found in Appendix A. Figure 4.7 shows the O_2 mixing ratio as a function of the specific energy for Tube A. Although the specific energy was varied over a broad range through different parameters (measurements were done under pulsed and non-pulsed conditions where pressure, flow or residence time were kept constant), all measurements follow a same trendline. In all cases, the formation of O_2 seems to be uniformly determined by the specific energy. However, the mixing ratio seems slightly pressure dependent, where a larger pressure results in smaller molecular oxygen production. Possible explanations for this will be discussed later on. Also, one should note that the mixing ratio as function of the specific energy reprensents a straight line in a double logarithmic plot.

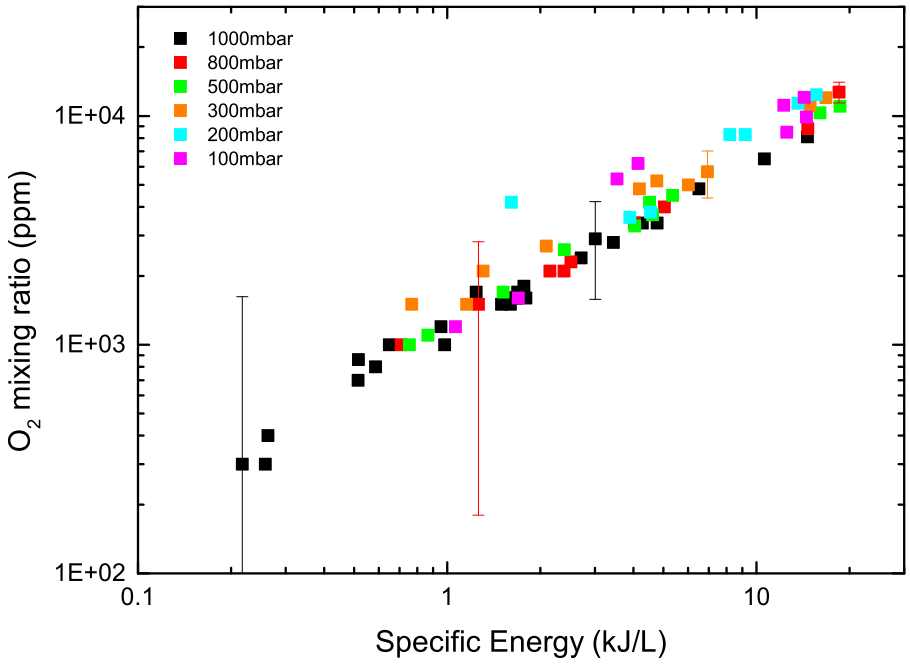

Figure 4.7.: Oxygen mixing ratio in ppm as function of specific energy combined from multiple measurement series on Tube A. These series include measurements under pulsed and non-pulsed conditions for different pressures, while the residence time was systematically adjusted. To give some indication of the uncertainty, a few error bars are included.

Similarly, the experiments performed for Tube B with an increased discharge gap are summarised in Figure 4.8. The specific energy was changed between 0.8kJ/L and 15kJ/L, i.e. in a similar range as for Tube A. Also, for measurements on Tube B, the specific energy was varied via pressure, flow rate and duty cycle while keeping other process parameters constant. Despite the difference in active discharge volume, both tubes show a similar trendline. Tube B also produces a straight line when plotting oxygen mixing ratio as a function of the specific energy.

An increased scatter of data can be seen in Figure 4.8 which almost exceeds the error bars, for example for two data points at 800mbar with a specific energy of about 3.0kJ/L. These data points were measured at a flow of 1245sccm. At these high flows, the plasma often does not fill the entire reactor volume. Therefore, the same amount of power is injected in

a smaller volume. Since the calculation of the specific energy is based on the assumption that the whole reactor volume is ignited, this results in an underestimated specific energy. In case only half of the reactor volume is ignited, the effective specific energy would increase by a factor of two, which would be in better agreement with the general trend. This effect makes it possible to make an estimation of the amount of reactor volume that is occupied by plasma.

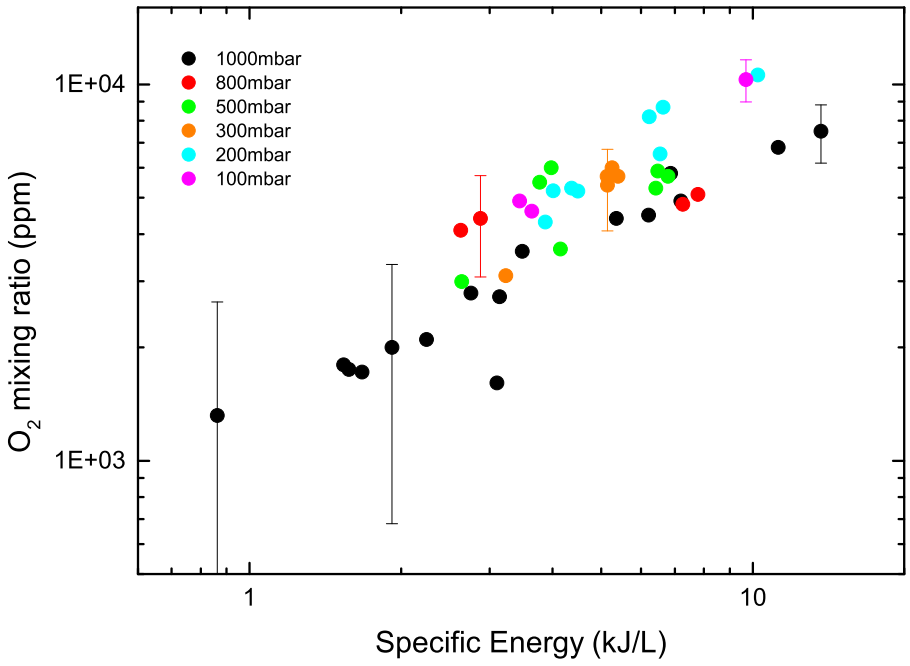

Figure 4.8.: Oxygen mixing ratio in ppm as function of specific energy combined from multiple measurement series on Tube B. These series include measurements with varying pressure, varying residence time, flow, duty cycle, etc. The measurements are seperated by pressure to be able to identify pressure dependence in the measurement as observed in earlier studies. To give some indication of the uncertainty, a few error bars are included.

To check the statement that both tubes have similar oxygen production, the results from Figure 4.7 and Figure 4.8 are combined in one graph (Figure 4.9). From this figure, it becomes clear that both tubes have similar characteristics in terms of CO production. The tube with the smaller gap (Tube A) has a larger specific energy range, mostly because igniting a plasma is easier with the smaller gap, therefore being able to go more to the 'extremes'. In the specific energy range where measurements were performed for both tubes, the data points seem to be on a joined trendline.

From this, it can be concluded that the different volume to surface ratio of Tube B does not affect total oxygen production considerably, although it may be of influence for the slight pressure dependence of oxygen production mentioned earlier. This effect can be caused by the temperature dependence of the O_3 production. Usually reduced O_3 mixing ratios are observed for plasma conditions which produce relatively high reactor temperatures (e.g. low flow ratios, 100% duty cycle etc.). Because the flow tube is not actively cooled, a change in pressure will correspond to a change in temperature, thus making the O_3 mixing ratio pressure dependent. Because the O_3 and O_2 are linked through Equation 4.1, the O_2 mixing ratio will also be pressure dependent. However, because the O_3 production is relatively small compared to the O_2 production, this effect would result in a very marginal pressure dependence in the O_2 mixing ratio.

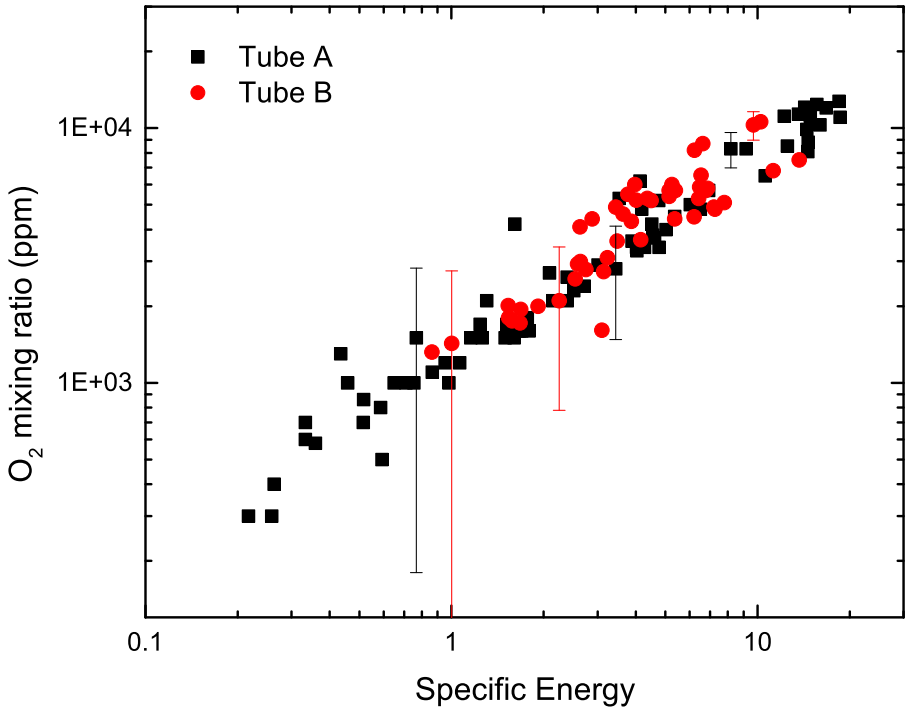

Figure 4.9.: Oxygen mixing ratio in ppm as function of specific energy combined from multiple measurement series on both tubes. To give some indication of the uncertainty, a few error bars are included.

It is interesting to compare the uniform trend established for the oxygen concentrations as function of specific energy for different reactors and plasma conditions with the mixing ratios of other stable reaction products like CO and O_3. These molecules were measured for the purpose of calculating the oxygen balance. Additionally, the CO conversion efficiency can be determined and is between 0.01% and 3%. Also, the oxygen-to-CO-ratio can be calculated and is found to be almost constant at 50% as can also be seen in Figure 4.10. This implies that the CO_2 conversion mainly occurs via $CO_2 \rightarrow CO + \frac{1}{2} O_2$. The ozone mixing ratio is relatively low, typically between 10 and 100 ppm. The large scattering of data points in the ozone are not related to large uncertainties, but is very likely the result of a strong temperature dependence of the ozone production. However, because these mixing ratios are relatively low, they don't affect the oxygen mixing ratio significantly. In other words, the results clearly show that although the ratio between CO and O_2 production is approximately 2:1, this does nog suggest that ozone is not formed in the plasma.

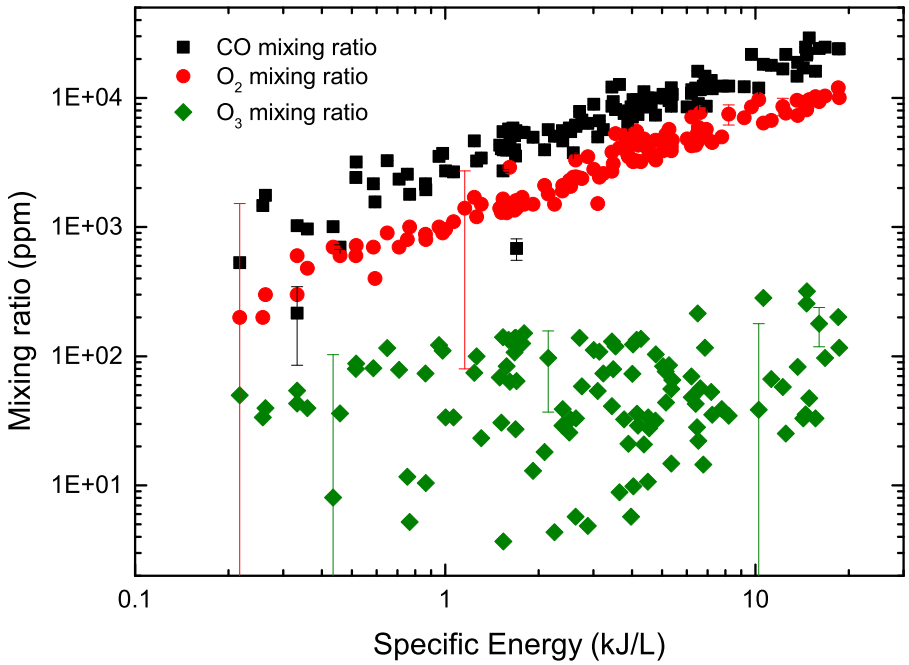

Figure 4.10.: Carbonmonoxide, molecular oxygen and ozone mixing ratios in ppm (all measured) as function of specific energy combined from multiple measurement series on both tubes. To give some indication of the uncertainty, a few error bars are included. Note that error bars for carbonmonoxide are included, however, these are generally too small to be visible.

5. Summary

The goal of this project was to determine the amount of molecular oxygen produced by an atmospheric pressure dielectric barrier discharge in a CO_2 gas. This discharge is generated inside a quartz glass flow tube with two parallel plates spanning the active region of the DBD. Measurements were done on tubes with a gap of 1mm and a gap of 3mm. Both tubes have similar oxygen production as function of the specific energy.

This oxygen production is measured using Tunable Diode Laser Absorption Spectroscopy (TDLAS) on an absorption line pair in the oxygen A-band ($b^1\Sigma_g^+ \leftarrow X^3\Sigma_g^-$), at wavelengths of 764.17nm and 764.28nm. Both oxygen lines are fit seperately by the software used, resulting in two independent values for the oxygen mixing ratios. Values were found between 0.03% and 1.27%, which is in good agreement with estimates based on the oxygen balance of the chemical system. The oxygen balance was established from simultaneous measurements of the CO and O_3 mixing ratios by FTIR spectroscopy. Under the assumption that only CO, O_2 and O_3 are produced by the DBD, this also results in oxygen mixing ratios.

It is found that the oxygen mixing ratio is weakly pressure dependent, where higher pressures result in slightly lower oxygen production than for lower pressures. This effect seems to happen in both flow tubes, and is observed in both TDLAS and FTIR measurements. Unfortunately, the reactor temperature also changes when the pressure is varied, making it difficult to disentangle pressure and temperature dependence. From the measurements, it is not conclusive whether the variance in oxygen production is due to pressure/temperature dependence of the CO production or O_3 production. The cause for the pressure/temperature dependence is still subject to further research.

For atmospheric pressure, the uncertainty for the FTIR measurements is about 30 times smaller than for the TDLAS meausurement, which is mainly attributed to CO and O_3 having much larger line strengths than oxygen absorption lines in the A-band. At lower pressures (100mbar), the uncertainties in FTIR measurements are about 3 times smaller than the uncertainties in TDLAS measurements. The uncertainty in the TDLAS measurements is mostly attributed to a curvature in the baseline due to small mechanical fluctuations in the laser diode. This results in an overestimation of one of the measured mixing ratios while the other mixing ratio is slightly underestimated. A slight reduction of this uncertainty could be achieved by choosing a more appropriate averaging time for the TDLAS measurements.

Although the FTIR measurements are more precise than the TDLAS measurements, the main advantage of TDLAS is that the results are available in realtime, whilst for the FTIR, a lot of analysis (post-treatment) has to be done. Because the results are available in realtime, it is easy to see from the oxygen mixing ratios when the plasma activation process stabilizes in terms of temperature and pressure. This provides an indirect monitoring system for the efficiency of the plasma activation process. Furthermore, this system can be used to estimate the amount of reactor volume filled with plasma, which could not be achieved using any of the other diagnostic tools in the setup. This however can not be done in realtime.

Broadly speaking, the assumption that only CO, O_2 and O_3 are formed as stable products in the DBD was verified. Furthermore, the CO:O_2 ratio of about 2:1 indicates that recombination into molecular oxygen dominates and hampers further CO_2 dissociation.

A. Additional results

Any results that are not included in the results section are placed here for completeness. The captions of each graph explain which conditions were used.

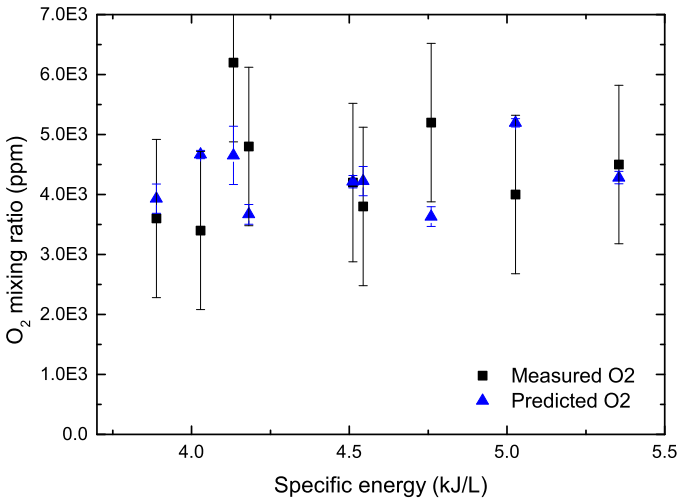

Figure A.1.: Oxygen mixing ratio as function of specific energy for Tube A. In this measurement, a constant flow of 518sccm is used, while the pressure is varied between 120mbar and 800mbar. This measurement is not pulsed (e.g. it has a duty cycle of 100%).

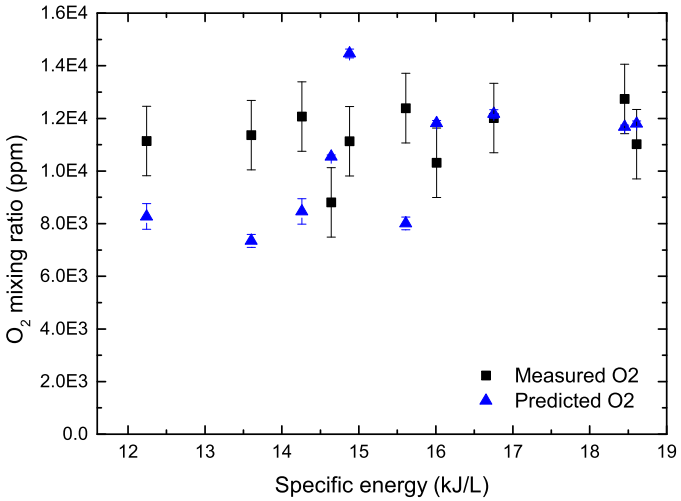

Figure A.2.: Oxygen mixing ratio as function of specific energy for Tube A. In this measurement, a constant flow of 148sccm is used, while the pressure is varied between 120mbar and 800mbar. This measurement is not pulsed (e.g. it has a duty cycle of 100%).

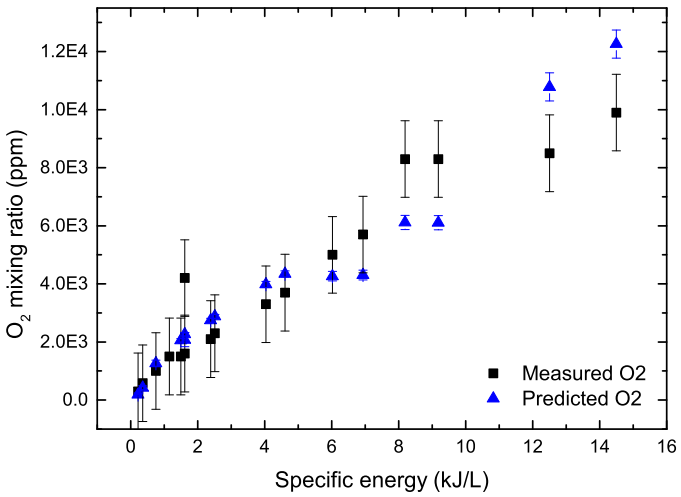

Figure A.3.: Oxygen mixing ratio as function of specific energy for Tube A. In these measurements, the pressure is varied betweem 120mbar and 1000mbar. The flow was adjusted between 134sccm and 1200 sccm to maintain a constant residence time of 100ms. For each value of a specific flow and pressure, three measurements are done using different duty cycles.

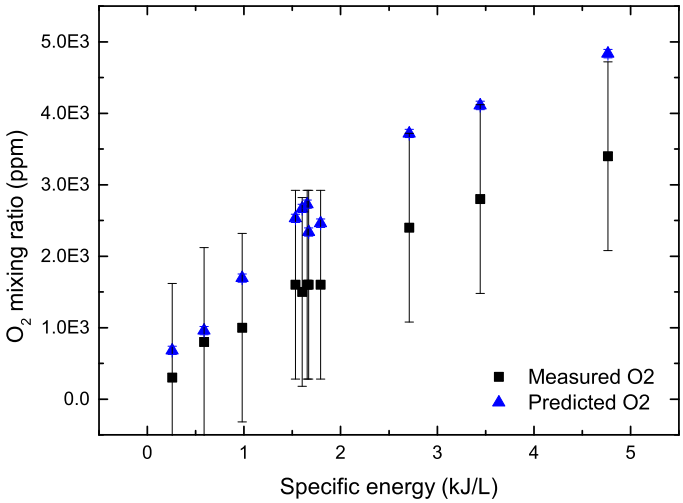

Figure A.4.: Oxygen mixing ratio as function of specific energy for Tube A. In this measurement, a constant flow of 518sccm is used and the pressure is kept consant at 1000mbar, thus also keeping the residence time constant. Only the duty cycle is varied between 9% and 100%. The four closely spaced data points in this graph are all points with a duty cycle of 44%, where only the absolute value of the on- and off-period are increases, keeping their ratio the same.

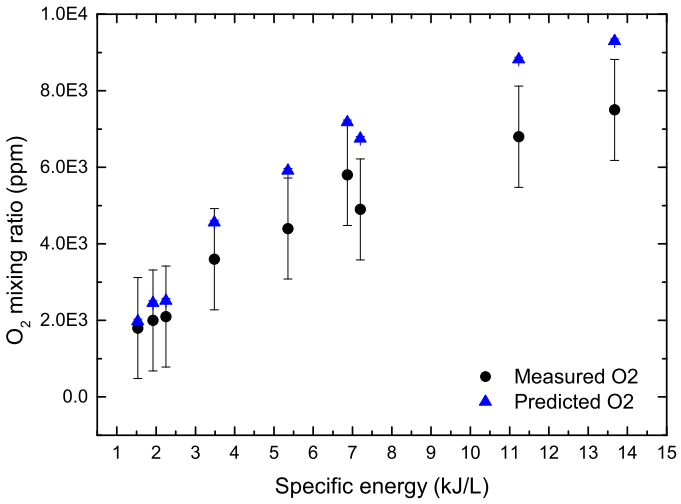

Figure A.5.: Oxygen mixing ratio as function of specific energy for Tube B. The pressure for this measurement was kept constant at a 1000mbar, while the flow was varied between 234sccm and 1560sccm. This measurement is not pulsed (e.g. it has a duty cycle of 100%).

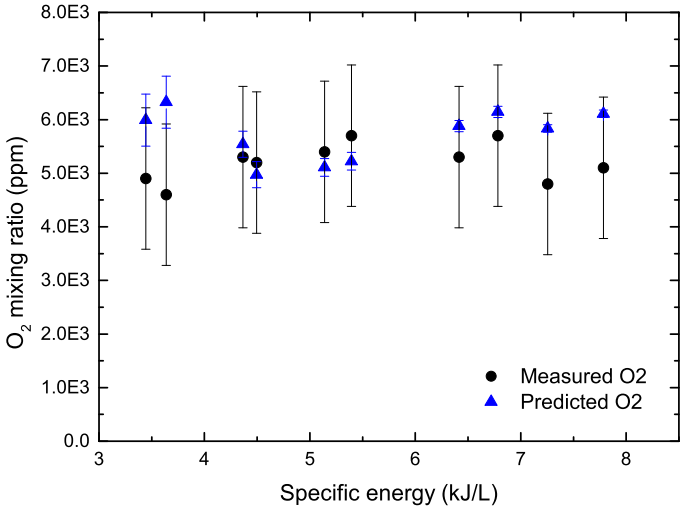

Figure A.6.: Oxygen mixing ratio as function of specific energy for Tube B. The flow for this measurement was kept constant at 450sccm, while the pressure was varied between 120mbar and 800mbar. This measurement is not pulsed (e.g. it has a duty cycle of 100%).

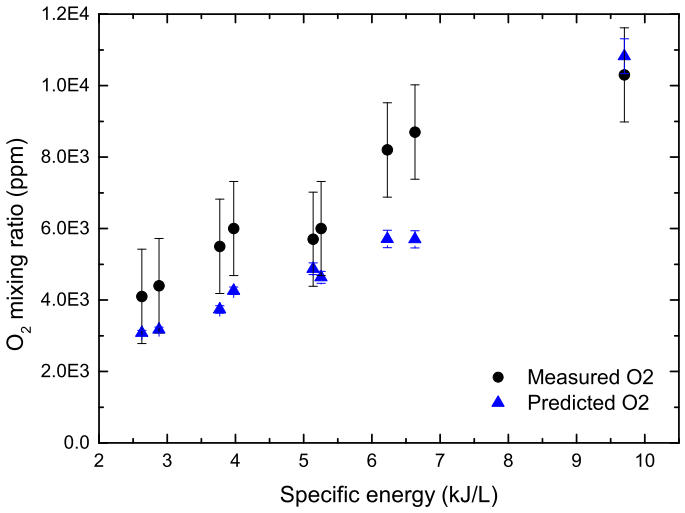

Figure A.7.: Oxygen mixing ratio as function of specific energy for Tube B. The residence time for this measurement was kept constant at 231ms, while the pressure and flow were varied between respectively 100mbar and 800mbar and 156sccm and 1245sccm. This measurement is not pulsed (e.g. it has a duty cycle of 100%).

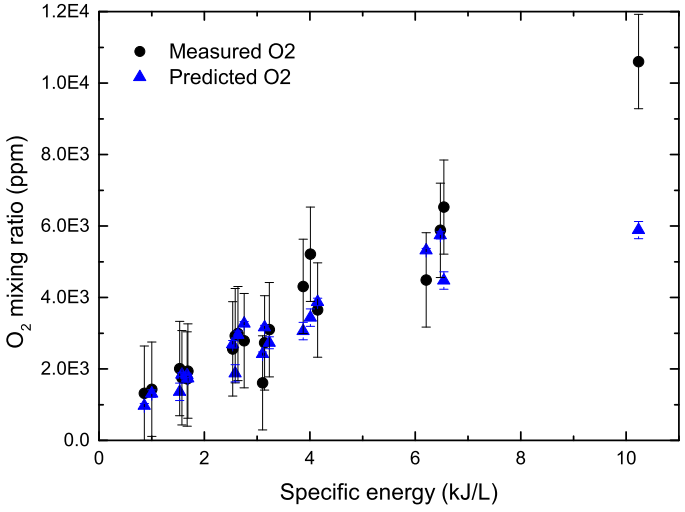

Figure A.8.: Oxygen mixing ratio as function of specific energy for Tube B. Measurements were done for residence times of 160ms, 400ms and 800ms. For this, varying pressures between 200mbar and 1000mbar were used, while the flow was between 181sccm and 1126sccm. For each condition pair, three measurements with different duty cycles were done (respectively 29%, 50% and 100%).

B. FTIR analysis

The analysis of the FTIR results is done by a script written in MATLAB. The software makes use of Equation 2.5, where $k(\nu)$ is used for an absorption line caused by a species labeled j and thus $k(\nu) = n_j\sigma_j(\nu)$. The script uses a reference spectrum for the to-be-analysed species with a mixing ratio of $x = n_k/n_0$, which can be generated using the Q-MACSoft-HT software. This reference spectrum is described by:

$$\left(\frac{I(\nu)}{I_0(\nu)}\right)_{ref} = \exp^{-\sigma_j(\nu)n_k L} \tag{B.1}$$

Note that this profile is pressure dependent for a fixed number of parts per million. The script now guesses a profile, for a mixing ratio of $\alpha x = n_l/n_0$, which can be descibed using the equation:

$$\left(\frac{I(\nu)}{I_0(\nu)}\right)_{guess} = \exp^{-\sigma_j(\nu)n_l L} = \left(\exp^{-\sigma_j(\nu)n_k}\right)^{\alpha} \tag{B.2}$$

where α is defined as n_l/n_k. For example, squaring every data point in this reference spectrum (thus $\alpha = 2$) would give a spectrum for the species with a mixing ratio of $2x$. This concept is exploited by the analysis software. It generates spectra for a large number of mixing ratio from 100 times smaller than the reference measurement up to 100 times larger (e.g. $0.01 \leq \alpha \leq 100$). The software then compares these guessed spectra with the measured spectrum by first interpolating the data so that the data and reference contain the same amount of data points. After this, a least square analysis is performed using the equation:

$$d(f) = \frac{\sum_{i=1}^{N}(y_i - (r_i)^{\alpha})^2}{N} \tag{B.3}$$

where y_i is the value of i'th data point of the measured data set, r_i is the value of i'th data point of the reference data set, α is the factor with which the reference data set mixing ratio is multiplied in the current loop, N is the number of data points in the data and reference sets and d a value representing the difference between the current guessed spectrum and the data set. When d is plotted as a function of α, a minimum occurs somewhere, indicating that the best correspondance between data sets is obtained at α_{best}, thus giving an value for the mixing ratio of $\alpha_{best}x$ where x is the mixing ratio in the reference data set. For extra precision, the minimum in the d as function of α graph is fitted using a second order polynomial $p(\alpha)$, where the minimum of $p(\alpha)$ is taken as α_{best}, because it is then also possible to get values for the mixing ratio in between data points for α as generated by the software. Ideally, the software would return a value for the number density of $n_l = n_j$.

This concept is applied to multiple species and multiple measurements, where an array of measurements and corresponding pressures should be given, together with wavenumber ranges on which the software should fit the reference data sets. The code used for analysis can be found below.

run.m

```
format long e

% define
data_dir = 'D:\Documents\School\2012-2013\Stage PMP\Analysis\FTIR\Baseline ...
    Corrected FTIR\130606\300\';
reference_dir = 'D:\Documents\School\2012-2013\Stage PMP\Analysis\FTIR\Hitran ...
    Data\Lowres\'; % instrumental broadening of 0.25 cm-1, maybe even more
results_dir = strcat(data_dir, 'Results\');
results_file = strcat(results_dir, 'results_309_to_312.txt');

% get a list of data files
data_files = dir(strcat(data_dir, '*_all.txt'));

% species array
species = cell(2,1);
species{1} = 'CO';
species{2} = 'O3';

% for very high CO concentrations, 2039-2049 cm-1 is a good fitting range
% for relatively high CO concentrations, 2049-2059 cm-1 is a very good ...
    fitting range
% for relatively low CO concentrations, 2138-2150 cm-1 is a good fitting range

% variables should contain the following columns:
% 1: species name
% 2: start wavenumber for filename
% 3:  end wavenumber for filename
% 2: start wavenumber for actual fit
% 3:  end wavenumber for actual fit
% 4: ppm in reference data
references = zeros(2, 6);
references(1, :) = [1, 2020, 2250, 2138, 2150, 1000000];
references(2, :) = [2, 1058, 1061, 1058.5, 1060.5, 10000];

% measurements array, coupling measurement number to pressure in mbar
measurements = zeros(4, 2);
measurements(1, :) = [309, 200];
measurements(2, :) = [310, 200];
measurements(3, :) = [312, 120];
measurements(4, :) = [313, 120];

% reserve space for the results of the analysed data
results = zeros(length(measurements(:, 1)), 1+length(references(:, 1)));
results(:, 1) = measurements(:, 1);

% loop through the data files and analyse them
for i=1:length(measurements(:, 1))
    % retrieve the data number
    data_number = measurements(i, 1);

    % retrieve the filename
    filename = sprintf('0%d.0_all.txt', data_number);

    % import the file and retrieve the file data
    imported_file = importdata(strcat(data_dir, filename));
    file_data = imported_file.data;

    for j=1:length(references(:,1))
        % get the species name
        species_name = species{j};
```

```
58
59          measurements_array_index = find(measurements(:, 1) == data_number);
60          measurement_pressure = measurements(measurements_array_index, 2);
61
62          reference_filename_from_wavenumber = references(j, 2);
63          reference_filename_to_wavenumber = references(j, 3);
64          reference_fit_from_wavenumber = references(j, 4);
65          reference_fit_to_wavenumber = references(j, 5);
66          reference_ppb = references(j, 6);
67          reference_filename = sprintf('%s_%dmbar_%dppb_%d_%d.asc', ...
                species_name, measurement_pressure, reference_ppb, ...
                reference_filename_from_wavenumber, ...
                reference_filename_to_wavenumber);
68          fprintf('Using file %s as reference\n', reference_filename);
69
70          % import the reference data
71          reference_data = importdata(strcat(reference_dir, reference_filename));
72
73          % analyse the CO concentration and store a graph to check if the fit is
74          % good enough
75          [ppb, plot_handle, fit_handle] = get_ppb(data_number, file_data, ...
                species_name, reference_data, reference_ppb, ...
                reference_fit_from_wavenumber, reference_fit_to_wavenumber);
76          print(plot_handle, '-dpng', sprintf('%s%d_%s_plot.png', results_dir, ...
                data_number, species_name));
77          print(fit_handle, '-dpng', sprintf('%s%d_%s_fit.png', results_dir, ...
                data_number, species_name));
78          fprintf('The sample numbered %d contains about %d ppb of %s\n', ...
                data_number, ppb, species_name);
79
80          results(i, 1+j) = ppb;
81      end;
82  end;
83
84  dlmwrite(results_file, results, 'delimiter', '\t', 'precision', 6);
```

findclosest.m

```
1  function[index] = findclosest(array,value)
2      temp = value * ones(length(array), 1);
3      diff = abs(array - temp);
4      [minimum, index] = min(diff);
5  end
```

get_ppb.m

```
1  function[ppb, plot_handle, fit_handle] = get_ppb(data_number, data_set, ...
       reference_species, reference, reference_ppb, fit_from_wavenumber, ...
       fit_to_wavenumber)
2      % reserve variable that stores the average differences for every factor
3      % and some counters
4      factor_range = logspace(-2, 2, 1000);
5      averages = zeros(length(factor_range), 2);
6
7      % select the desired data for the used range
8      fit_data_start_index = findclosest(data_set(:,1), fit_to_wavenumber); % ...
           note, the scale for the data is reversed, hence the max for the start ...
           index
9      fit_data_end_index = findclosest(data_set(:,1), fit_from_wavenumber);
10
```

```
11      % select the fit and plot data according to the indexes calculated above
12      fit_data = [data_set(fit_data_start_index:fit_data_end_index, 1), ...
            data_set(fit_data_start_index:fit_data_end_index, 4)];
13
14      % a linear counter for the loop following
15      factor_counter = 1;
16
17      % interpolate the measured data to have the same distribution of
18      % data points as the reference data
19      yi = interp1(fit_data(:,1), fit_data(:,2), reference(:,1));
20
21      % try a lot of factors
22      for factor=factor_range
23          % calculate the reference spectrum for the given factor
24          current_pass_reference = [reference(:,1), reference(:,2).^factor];
25          current_pass_reference(:,2) = current_pass_reference(:,2);
26
27          % calculate the mean difference between the measurements
28          mean = nanmean((yi - current_pass_reference(:,2)).^2);
29          averages(factor_counter, :) = [factor, mean];
30
31          % update the counter
32          factor_counter = factor_counter+1;
33      end;
34
35      % get the factor with the minimum difference
36      [min_diff, best_factor_index] = min(averages(:, 2));
37      best_factor = averages(best_factor_index, 1);
38
39      % define a second order shifted polynomial to fit the averages curve
40      F = @(param,xdata)param(2).*(xdata-param(1)).^2 + param(3);
41      x0 = [best_factor 0.001 min_diff];
42      options = optimset('Display','off');
43
44      % fit 7 data points for the fit, surrounding the minimum of the average
45      % difference
46      polynomial_fit_start_index = best_factor_index - 3;
47      polynomial_fit_end_index = best_factor_index + 3;
48
49      % if the polynomial is fit near the edge, correct out of bounds indices
50      if polynomial_fit_start_index < 1
51          polynomial_fit_start_index = 1;
52      end
53
54      if polynomial_fit_end_index > length(averages(:,1))
55          polynomial_fit_end_index = length(averages(:,1));
56      end
57
58      % fit the curve and retrieve the minimum x value of the fit
59      [p,resnorm,residual] = lsqcurvefit(F, x0, ...
            averages(polynomial_fit_start_index:polynomial_fit_end_index, 1), ...
            averages(polynomial_fit_start_index:polynomial_fit_end_index, 2), [], ...
            [], options);
60      best_factor = p(1);
61
62      % plot the differences as function of the factor
63      fit_handle = figure('visible','off');
64      plot(averages(polynomial_fit_start_index:polynomial_fit_end_index, 1), ...
            averages(polynomial_fit_start_index:polynomial_fit_end_index, 2), ...
            averages(polynomial_fit_start_index:polynomial_fit_end_index, 1), ...
            F(p,averages(polynomial_fit_start_index:polynomial_fit_end_index, 1)));
65
66      % calculate the indexes for the reference of what to plot so that the
```

```
67      % same range is achieved as for the fit data
68      reference_plot_start_index = findclosest(reference(:,1), min(fit_data(:, ...
            1)));
69      reference_plot_end_index = findclosest(reference(:,1), max(fit_data(:, 1)));
70
71      % plot the original data and reference data in one graph
72      plot_handle = figure('visible','off');
73      plot(fit_data(:,1), fit_data(:,2), ...
            reference(reference_plot_start_index:reference_plot_end_index, 1), ...
            reference(reference_plot_start_index:reference_plot_end_index, ...
            2).^best_factor);
74
75      % calculate the ppm and display it
76      ppb = round(reference_ppb * best_factor);
77  end
```

Bibliography

[1] N.S. Lewis and D.G. Nocera. Powering the planet: Chemical challenges in solar energy utilization. *PNAS*, 103(43), 2006.

[2] R.E. Smalley. Future global energy prosperity: The terawatt challenge. *MRS Bulletin*, 30(6):412–417, 2005.

[3] Z. Jiang, T. Xiao, et al. Turning carbon dioxide into fuel. *Phil. Trans. R. Soc. A*, 368, 2010.

[4] A. Lebouvier, S.A. Iwarere, et al. Assessment of carbon dioxide dissociation as a new route for syngas production: A comparative review and potential of plasma-based technologies. *Energy Fuels*, 27, 2013.

[5] O. Varghese, M. Paulose, T. LaTempa, and C. Grimes. High-rate solar photocatalytic conversion of co2 and water vapor to hydrocarbon fuels. *Nano Letters*, 9:731–737, 2009.

[6] V. D. Rusanov, A. A. Fridman, and G. V. Sholin. The physics of a chemically active plasma with nonequilibrium vibrational excitation of molecules. *Uspekhi Fizicheskikh Nauk*, 134:185–235, 1981.

[7] S. Paulussen, B. Verheyde1, X. Tu, et al. Conversion of carbon dioxide to value-added chemicals in atmospheric pressure dielectric barrier discharges. *Plasma Sources Science and Technology*, 19, 2010.

[8] U. Kogelschatz. Dielectic-barrier discharges: Their history, discharge physics, and industrial applications. *Plasma Chemistry and Plasma Processing*, 23, 2003.

[9] R. Aerts, T. Martens, and A. Bogaerts. Influence of vibrational states on co2 splitting by dielectric barrier discharges. *The Journal of Physical Chemistry*, 116, 2012.

[10] B. Eliasson, W. Egli, and U. Kogelschatz. Modelling of dielectric barrier discharge chemistry. *Pure and Applied Chemistry*, 6:1275–1286, 1994.

[11] L.S. Rothman, I.E. Gordon, et al. The hitran 2008 molecular spectroscopic database. *Journal of Quantitative Spectroscopy & Radiative Transfer*, 110:533–572, 2009.

[12] L.S. Rothman, C.P. Rinsland, et al. The hitran molecular spectroscopic database and hawks (hitran atmospheric workstation): 1996 edition. *Journal of Quantitative Spectroscopy & Radiative Transfer*, 60:665–710, 1998.

[13] L.S. Rothman, D. Jacquemarta, et al. The hitran 2004 molecular spectroscopic database. *Journal of Quantitative Spectroscopy & Radiative Transfer*, 96:139–204, 2005.

[14] J.B. McManus, P.L. Kebabian, and M.S. Zahniser. Astigmatic mirror multipass absorption cells for long-path-length spectroscopy. *Applied Optics*, 34(18), 1995.

[15] J.B. McManus, M.S. Zahniser, and David D. Nelson. Dual quantum cascade laser trace gas instrument with astigmatic herriott cell at high pass number. *Applied Optics*, 50(4), 2011.

[16] P. Werle. Accuracy and precision of laser spectrometers for trace gas sensing in the presence of optical fringes and atmospheric turbulence. *Applied Physics B*, 102:313–329, 2011.

[17] D.W. Allan. Statistics of atomic frequency standards. *Proceedings of the IEEE*, 52(2):211–230, 1966.

[18] J.A. Barnes. Atomic timekeeping and the statistics of precision signal generators. *Proceedings of the IEEE*, 54(2):207–220, 1966.